Journal of Sound and Vibration (2002) **250**(3), 519–539
doi:10.1006/jsvi.2001.3935, available online at http://www.idealibrary.com on IDEAL®

PASSIVE DAMPING AUGMENTATION OF A VIBRATING BEAM USING PSEUDOELASTIC SHAPE MEMORY ALLOY WIRES

F. GANDHI† AND G. CHAPUIS

Department of Aerospace Engineering, The Pennsylvania State University, 229 Hammond Building, University Park, PA 16802, U.S.A. E-mail: fgandhi@psu.edu

(*Received* 18 *December* 2000, *and in final form* 25 *July* 2001)

This paper examines the effectiveness of pseudoelastic shape memory alloy (SMA) wires for passive damping of flexural vibrations of a clamped–free beam with a tip mass. A finite-element model of the system is developed and validated with experimental results. The SMA behavior is modelled using amplitude-dependent complex modulus. Numerical simulations indicate that the damping introduced by the SMA wires will increase for higher excitation-force amplitudes that produce higher strain levels in the SMA wires. Increasing the wire cross-section area provides more damping at low force-excitation amplitudes, but reduced damping at higher amplitudes. The angle between the beam and the SMA wires is an influential parameter, and a value in the 10–20° range was found to introduce maximum damping. The underlying physical mechanisms are examined in detail. System damping depends only mildly on the SMA wire length, and is unaffected by the tip mass.

1. INTRODUCTION

Nickel–titanium (Ni–Ti) shape memory alloys (SMAs) are known to exhibit stress/strain pseudoelastic hysteresis associated with *stress-induced* austenite–martensite phase transformations, when subjected to cyclic stress/strain loadings above a critical temperature (the austenite finish temperature). Distinct from the more commonly used shape memory effect (whereby *temperature-induced* phase transformations are exploited for use in low-frequency actuators), pseudoelastic hysteresis of SMAs can potentially be exploited for *passive* damping augmentation in various mechanical, civil, and aerospace applications. A damper can be designed with SMA wires pre-stressed (or pre-strained) to a level somewhere in the middle of the pseudoelastic range [1]. Cyclic variations in stress and strain around the baseline, as the system undergoes vibration, will then result in energy dissipation due to hysteresis in the SMA.

If SMAs are integrated into structures, they would have several potential advantages over traditional damping materials such as elastomers. For example, the energy dissipated per unit volume (a measure of damping capacity) is much higher than that provided by commonly used elastomeric materials [2]. Additionally, available damping from elastomers can reduce significantly at low temperatures, compromising damper performance in critical systems. Since SMA damper temperature can be controlled by electrical heating, degradation in performance due to temperature variation can be avoided. Clearly, high

† Member AIAA, AHS.

0022-460X/02/080519 + 21 $35.00/0

damping capacity and controllability of SMA-based damping systems make them attractive candidates for structural damping augmentation. In recent years, some studies have already been reported demonstrating the use of pseudoelastic SMAs for passive structural damping augmentation (see for example references [3–8]). However, many of these studies have assumed an overly simplified SMA hysteresis behavior (often due to lack of suitable models), and do not focus on several fundamental issues such as the impact of the SMA damper configuration or excitation amplitude on system damping.

In recent years, there have also been continued efforts in SMA material characterization and development of constitutive models suitable for structural dynamics applications. In particular, there has been emphasis on experimentally determining the SMA pseudoelastic hysteresis behavior over a range of excitation frequencies. With hysteresis data previously reported only at very low strain rates (quasi-static conditions), unsuitable for vibration damping applications, the first author and co-workers experimentally characterized the SMA hysteresis behavior up to frequencies of 10 Hz [2, 9]. There has also been an emphasis on development of simple yet accurate SMA constitutive models that can be easily integrated into structural finite-element analyses. From this standpoint, thermodynamic-based SMA constitutive models [10–13] that require calculation of martensite–austenite phase fractions and transformations as a function of stress and temperature, have limited appeal. A better approach is to characterize SMAs using the *complex modulus*. The complex modulus approach, frequently used in structural dynamics for characterizing damping materials [14–16], comprises a storage modulus (representative of stiffness) and a loss modulus (representative of damping), both of which are frequency- and temperature-dependent. In addition, for non-linear materials the complex modulus also varies with excitation amplitude [17–19]. A complex modulus representation of SMA behavior, as presented in reference [20], can be easily integrated into structural analyses, and influence of the SMA on structural response or modal damping can then be readily calculated.

The detailed characterization of SMA hysteresis behavior and availability of complex modulus representations thereof, provides a tremendous opportunity to develop finite-element analyses and conduct parametric studies to provide detailed physical insight, as well as optimization studies to evaluate the most effective SMA design configurations for structural damping augmentation.

2. OBJECTIVES AND APPROACH OVERVIEW

In the present study, a clamped–free vibrating beam with a tip mass and symmetrically mounted pseudoelastic SMA wires (schematic sketch shown in Figure 1) is considered to obtain a fundamental understanding of the influence of SMA damper configuration and system parameters, as well as operational parameters such as excitation force amplitudes on the performance of the SMA-based structural damping treatment.

The beam is subjected to a harmonic excitation force near the tip, and the bending response of the beam to this input excitation is calculated. An amplitude-dependent complex-modulus characterization of SMA hysteresis behavior is used, based on experimental data from references [9, 21]. On account of the non-linear behavior of the SMA wires, the beam periodic response is calculated iteratively, and damping in the fundamental mode of vibration is examined. After verifying the accuracy of the finite-element analysis through experimental validation, the excitation-force amplitude, SMA wire cross-section area, wire length, angle between the wires and the beam, and the tip mass are varied, and the influence of these variations on system damping is evaluated and physically explained.

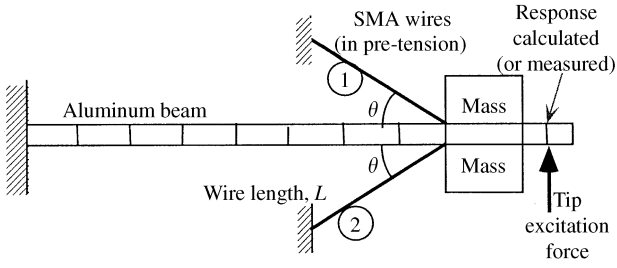

Figure 1. Schematic sketch of clamped–free beam with tip mass and symmetrically mounted pseudoelastic SMA wires to introduce damping of flexural vibrations.

3. ANALYTICAL MODEL AND SOLUTION SCHEME

To examine the effectiveness of the symmetrically mounted pseudoelastic SMA wires in introducing passive damping in the clamped–free beam with tip mass, a finite-element discretization of the system is carried out (Figure 1). The beam is assumed to undergo pure bending deformations with no extension or transverse shear (Euler–Bernoulli beam theory). The SMA wires are subjected to a pre-tension load, T. The angle between the wires and the undeformed beam is θ. The SMA behavior is described using a complex modulus. With the beam oscillating in the horizontal plane, the gravitational force on the tip mass is not considered. Section 3.1 describes the development of the finite-element equations of motion. This is followed by a description of the procedure used to calculate the system response under a tip harmonic excitation, $P = P_0 e^{j\omega t}$, in section 3.2 and a description of the method used to calculate the damping in section 3.3.

3.1. FINITE-ELEMENT EQUATIONS OF MOTION

In the finite-element analysis, the Euler–Bernoulli beam is spatially discretized into several elements, each having four degrees of freedom: w_1 and w_2 representing the transverse displacements at the left and right nodes, and w'_1 and w'_2 representing the slope at the two nodes. The transverse displacement within any element is then assumed to vary as a cubic function of the non-dimensional local co-ordinate, ξ $(0 \leqslant \xi \leqslant 1)$, and is related to the elemental degrees of freedom as

$$w = (1 - 3\xi^2 + 2\xi^3)w_1 + (\xi - 2\xi^2 + \xi^3)lw'_1 + (3\xi^2 - 2\xi^3)w_2 + (-\xi^2 + \xi^3)lw'_2, \quad (1)$$

where l is the length of the element. Using the above-assumed displacement function, the element stiffness and mass matrices can be obtained from expressions of the element strain energy and kinetic energy respectively.

3.1.1. *Beam element stiffness matrix*

The element bending stiffness matrix under the influence of a constant tensile force, F, is derived from the element strain energy, U:

$$U = \frac{1}{2}\int_{\substack{element\\length}} EI(w'')^2\,dx + \frac{1}{2}\int_{\substack{element\\length}} F(w')^2\,dx = \frac{1}{2}q^T K_1 q + \frac{1}{2}q^T K_2 q, \quad (2)$$

where

$$K_1 = \frac{EI}{l}\begin{bmatrix} 12 & 6l & -12 & 6l \\ 6l & 4l^2 & -6l & 2l^2 \\ -12 & -6l & 12 & -6l \\ 6l & 2l^2 & -6l & 4l^2 \end{bmatrix}, \quad K_2 = \frac{F}{l}\begin{bmatrix} 6/5 & l/10 & -6/5 & l/10 \\ l/10 & 2l^2/15 & -l/10 & -l^2/30 \\ -6/5 & -l/10 & 6/5 & -l/10 \\ l/10 & -l^2/30 & -l/10 & 2l^2/15 \end{bmatrix} \tag{3}$$

$$\text{and} \quad q = [w_1 \;\; w_1' \;\; w_2 \;\; w_2']. \tag{4}$$

In equation (3), the flexural stiffness, EI, would assume different values for the portions of the beam with and without the tip mass. The longitudinal force, F, is due to the pre-tension, T, in the SMA wires and can be shown to be $F = -2T\cos\theta$ (for portions of the beam inboard of the point of attachment of the wires). Then, the total element stiffness matrix is $K = K_1 + K_2$ for the portion of the beam under pre-compression, and $K = K_1$ for the portion of the beam outboard of the point of attachment of the wires.

3.1.2. *Beam element mass matrix*

The element mass matrix, M, is obtained from the element kinetic energy T:

$$T = \frac{1}{2}\int_{\substack{element\\length}} m(\dot{w})^2\,\mathrm{d}x + \frac{1}{2}\int_{\substack{element\\length}} \varsigma b(\dot{u})^2\,\mathrm{d}V. \tag{5}$$

In equation (5), m is the mass per unit length, ς is the mass density and b is the beam width. The first term represents the element translational kinetic energy due to transverse motion, and the second term represents the element rotational kinetic energy due to longitudinal motion. The element mass matrix due to translational kinetic energy, M_1, and the rotational kinetic energy, M_2, are given by

$$M_1 = \frac{ml}{420}\begin{bmatrix} 156 & 22l & 54 & -13l \\ 22l & 4l^2 & 13l & -3l^2 \\ 54 & -13l & 156 & -22l^2 \\ -13l & 3l^2 & -22l & 4l^2 \end{bmatrix},$$

$$M_2 = \frac{\alpha}{30}\begin{bmatrix} 36/l & -3 & -36/l & -3 \\ -3 & 4l & 3 & -l \\ -36/l & 3 & 36/l & 3 \\ -3 & -l & 3 & 4l \end{bmatrix}. \tag{6}$$

It should be noted that the mass per unit length, m, and the rotational interia, α, assume different values for the portion of the beam without the tip mass. The total element mass matrix is $M = M_1 + M_2$.

3.1.3. *Influence of SMA wires*

In section 3.1.1, the pre-tension in the SMA wires was shown to influence the stiffness matrix by subjecting the beam to a steady compressive force. In addition, the SMA wires undergo cyclic variations in strain due to the oscillations of the beam. The corresponding

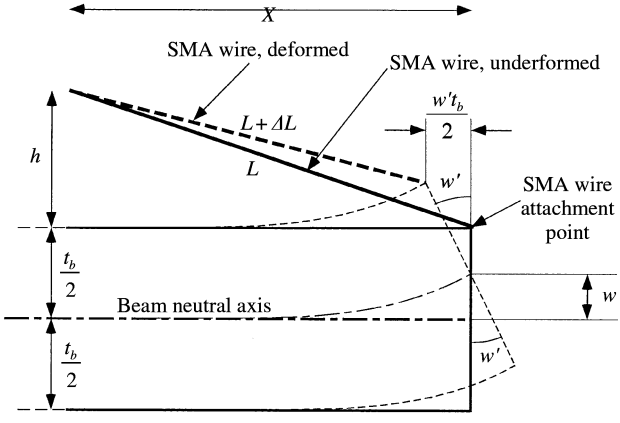

Figure 2. Schematic of SMA wire in deformed configuration.

changes in the SMA wire force directly act on the beam at the point of attachment. This section develops the equations to represent this effect.

Figure 2 shows one of the SMA wires (wire 1) in a deformed configuration due to the beam transverse deflection and rotation at the point of attachment. From the figure, the deformed length is

$$(L + \Delta L)^2 = (h - w_k)^2 + (X - w_k' t_b/2)^2. \tag{7a}$$

Further, the undeformed wire length can be expressed as

$$L^2 = h^2 + X^2. \tag{7b}$$

Subtracting equation (7b) from equation (7a) and neglecting the terms in ΔL^2, w_k^2, and $w_k'^2$ (which are of higher order),

$$2L\Delta \mathrm{L} = -2hw_k - 2Xw_k' t_b/2. \tag{8a}$$

Equation (8a) can be rewritten to obtain the net change in length:

$$\Delta L = -\frac{h}{L} w_k - \frac{X}{L}\frac{t_b}{2} w_k' = -\sin\theta\, w_k - \cos\theta \frac{t_b}{2} w_k'. \tag{8b}$$

Thus, the extensional strain in wire 1 associated with the beam deflection is

$$\varepsilon_1 = -\frac{\sin\theta}{L} w_k - \frac{\cos\theta}{L}\frac{t_b}{2} w_k'. \tag{9}$$

Similarly, it can be shown that the extensional strain in wire 2 is $\varepsilon_2 = -\varepsilon_1$. Using the complex modulus representation of SMA material behavior, the corresponding stresses in wire 1 and 2 are $\sigma_1 = (G' + \mathrm{j}G'')\varepsilon_1$ and $\sigma_2 = (G' + \mathrm{j}G'')\varepsilon_2 = -\sigma_1$. The forces in wire 1 can then be expressed as

$$F_1 = A(G' + \mathrm{j}G'')\varepsilon_1 = -\frac{A(G' + \mathrm{j}G'')}{L}(\sin\theta\, w_k + \cos\theta \frac{t_b}{2} w_k') \tag{10}$$

and the force in wire 2 is $F_2 = -F_1$. From the forces in individual wires, the net transverse force and moment exerted by both SMA wires on the beam is obtained. From Figure 3, the net transverse force is

$$F_Z = F_1 \sin\theta - F_2 \sin\theta = 2F_1 \sin\theta. \tag{11}$$

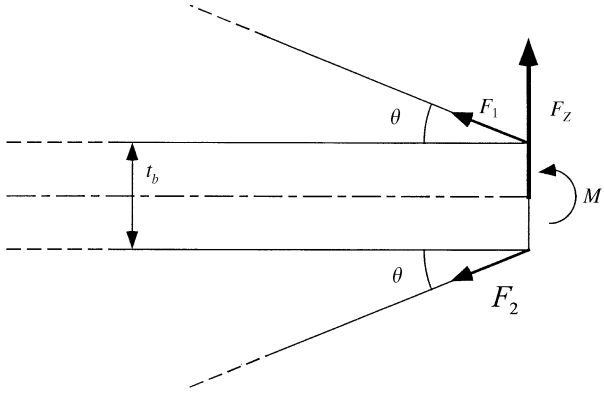

Figure 3. Force and moment exerted on the beam by the SMA wires at the point of attachment.

Introducing equation (10) into equation (11) yields

$$F_Z = -\frac{2A(G' + \mathrm{j}G'')}{L}\left(\sin^2\theta\, w_k + \sin\theta\cos\theta\frac{t_b}{2}w_k'\right). \tag{12}$$

From Figure 3, the net bending moment, M, is

$$M = F_1\cos\theta(t_b/2) - F_2\cos\theta(t_b/2) = 2F_1\cos\theta(t_b/2). \tag{13}$$

Introducing equation (10) into equation (13) yields

$$M = -\frac{2A(G'' + \mathrm{j}G'')}{L}(\sin\theta\cos\theta(t_b/2)w_k + \cos^2\theta(t_b/2)^2\, w_k'). \tag{14}$$

3.1.4. *Global equations of motion*

The element stiffness and mass matrices are assembled to obtain the global stiffness and mass matrices. After application of geometric boundary conditions the global finite-element equations of motion are expressed as

$$M^G\ddot{q}^G + K^G q^G = F^{SMA} + F^{ext}, \tag{15}$$

where K^G is the global stiffness matrix, M^G is the global mass matrix, q^G is the vector of global degrees of freedom, F^{SMA} represents the loads exerted on the beam by the SMA wires, and F^{ext} represents the external excitation on the system. In the present study, the external excitation comprises only a concentrated force acting near the beam tip (as seen in Figure 1). The only non-zero elements in F^{SMA} are the force F_Z (equation (12)) and moment M (equation (14)) at the node point where the SMA wires are attached to the beam.

Equations (12) and (14) can be represented in the form

$$\begin{Bmatrix} F_Z \\ M \end{Bmatrix} = -\frac{2A(G' + \mathrm{j}G'')}{L}\begin{bmatrix} \sin^2\theta & \sin\theta\cos\theta(t_b/2) \\ \sin\theta\cos\theta(t_b/2) & \cos^2\theta(t_b/2)^2 \end{bmatrix}\begin{Bmatrix} w_k \\ w_k' \end{Bmatrix}, \tag{16}$$

Since the loads exerted by the SMA wires on the beam are motion-dependent, they will have an influence on the global stiffness matrix. It should be noted that in the 2×2 matrix above, only the (1, 1) term retains significance (while the (1, 2), (2, 1) and (2, 2) terms become

negligible) for very slender beams (except for values of $\theta \to 0$). The global finite-element equations of motion are then written as

$$M^G \ddot{q}^G + (K' + \mathrm{j}K'')q^G = F^{ext}. \tag{17}$$

The augmented global stiffness matrix is now complex due to the complex modulus of the SMA wires.

3.2. SOLUTION OF EQUATIONS OF MOTION USING HARMONIC BALANCE

Since the complex modulus approach is used for characterization of the SMA behavior, the system is analyzed in the frequency domain. The response to the transverse excitation force, $P = P_0 \mathrm{e}^{\mathrm{j}\omega t}$, acting close to the beam tip, is calculated using the harmonic balance method. The applied force and the resulting response in equation (17) can be expressed as

$$F^{ext} = F_0 \mathrm{e}^{\mathrm{j}\omega t} \quad \text{and} \quad q^G = (q_r - \mathrm{j}q_i)\mathrm{e}^{\mathrm{j}\omega t}. \tag{18}$$

Using equation (18) in equation (17), it can be shown that

$$\begin{bmatrix} K' - \omega^2 M^G & K'' \\ K'' & -(K' - \omega^2 M^G) \end{bmatrix} \begin{Bmatrix} q_r \\ q_i \end{Bmatrix} = \begin{Bmatrix} F_0 \\ 0 \end{Bmatrix}$$

$$\text{or} \quad \begin{Bmatrix} q_r \\ q_i \end{Bmatrix} = \begin{bmatrix} K' - \omega^2 M^G & K'' \\ K'' & -(K' - \omega^2 M^G) \end{bmatrix}^{-1} \begin{Bmatrix} F_0 \\ 0 \end{Bmatrix}. \tag{19}$$

After calculating the system response (q_r and q_i) at any excitation frequency, ω, the amplitude, q_0, of the response at some desired nodal degree of freedom, k, near the beam tip can then be obtained as

$$q_0 = \sqrt{q_r(k)^2 + q_i(k)^2}. \tag{20}$$

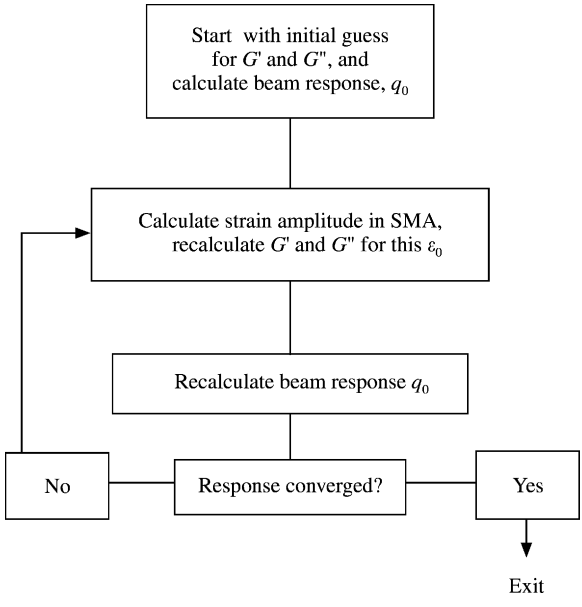

Figure 4. Flowchart depicting the iterative scheme used to calculate the system response.

It should be emhasized that since G' and G'' of the SMA wires are dependent on strain amplitude (which implies that K' and K'' in equation (17) and (19) depend on response amplitude), q_r and q_i have to be evaluated iteratively at any frequency. An estimated value of G' and G'' is used to first calculate q_r and q_i. With the beam displacement and slope then available at the point of attachment of SMA wires, the strain amplitude in the SMA wires can be calculated using equation (9). Based on this strain amplitude, an updated value of G' and G'' is now introduced and the process is repeated until convergence. A flowchart of this iterative solution procedure is shown in Figure 4. The compliance response function of the system, $H(\omega) = q_0(\omega)/p_0$, can then be obtained by calculating the response q_0 over a range of excitation frequencies.

3.3. EVALUATION OF SYSTEM DAMPING

After calculating the system response (as described in section 3.2), the modal damping can be evaluated. One measure of damping is the modal damping ratio calculated by applying the half-power bandwidth method to the compliance response function, $H(\omega)$. However, the half-power bandwidth method and the modal damping ratio are rigorously applicable only for linear systems. Alternatively, the modal loss factor, η, which represents a ratio of dissipated energy, D, to the maximum energy stored in a cycle, U_{max}, can be calculated. For a linear system, the modal loss factor *at resonance* condition is simply twice the modal damping ratio. In the present study, the modal loss factor at resonance is used as a quantitative measure of damping. It can be shown that the maximum stored energy in a cycle is given by [21]

$$U_{max} = \frac{1}{2}(q_r^{\mathrm{T}} K' q_r + q_i^{\mathrm{T}} K' q_i) \tag{21}$$

and the energy dissipated in a cycle, D, is given by [21]

$$D = \pi(q_r^{\mathrm{T}} K'' q_r + q_i^{\mathrm{T}} K'' q_i). \tag{22}$$

Alternatively, since energy is only dissipated in the SMA wires, the dissipated energy can be obtained by calculating the area inside the hysteresis loop:

$$D = (\int \sigma \, \mathrm{d}\varepsilon) V = \pi G'' \varepsilon_0^2 V, \tag{23}$$

where V is the wire volume and ε_0 is the SMA strain amplitude. The loss factor is then obtained as

$$\eta = \frac{1}{2\pi} \frac{D}{U_{max}}\bigg|_{\omega = \omega_r}. \tag{24}$$

In equation (24), U_{max} is the sum of the energy stored in the SMA wires (U_{SMA}) and in the beam. Noting that $U_{SMA} = \frac{1}{2} G' \varepsilon_0^2 V$, and using the definition for SMA material loss factor, $\eta_{SMA} = G''/G'$, it can be shown that the modal loss factor of the system can be expressed in the form

$$\eta = (U_{SMA}/U_{max})|_{\omega = \omega_r} \eta_{SMA}. \tag{25}$$

4. SMA AMPLITUDE-DEPENDENT COMPLEX MODULUS

In section 3, the complex modulus approach is used to represent the SMA behavior in the finite-element formulation. The complex modulus, which is strongly amplitude-dependent

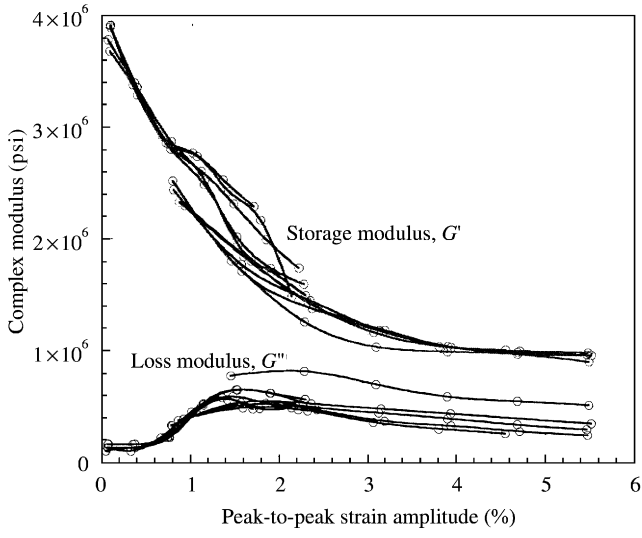

Figure 5. Compilation of data showing SMA complex modulus variation versus strain amplitude.

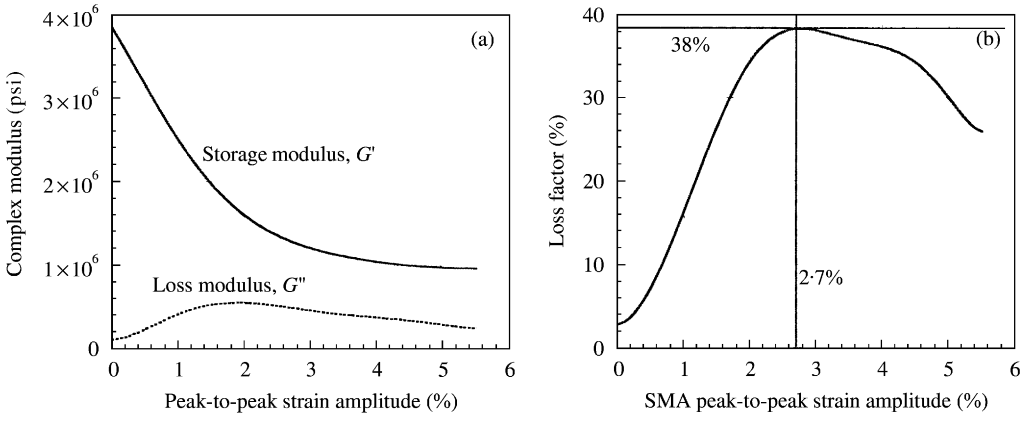

Figure 6. (a) Approximation of SMA complex modulus variation versus strain amplitude; (b) SMA wire (material) loss factor versus strain amplitude.

for SMAs, is calculated from hysteresis data obtained through cycling pre-strained SMA wires in an MTS machine. These tests, over a range of strain amplitudes and frequencies, are described in references [9, 21]. Figure 5 shows the variation of the storage modulus, G', and the loss modulus, G'', versus strain amplitude for several excitation frequencies. It is seen that storage modulus decreases for higher strain amplitudes, while the loss modulus displays a maximum at moderate strain amplitudes. Further, both storage and loss moduli show relatively small variations with changes in frequency (between 0·5 and 10 Hz). Therefore, for simplicity, the complex modulus is assumed to be invariant with the excitation frequency in this study. A "master-curve" (Figure 6(a)) is then generated using a least-square polynomial approximation [21] of the data in Figure 5. The variation of the SMA loss factor, $\eta_{SMA} = G''/G'$, versus strain amplitude, is shown in Figure 6(b).

5. RESULTS AND DISCUSSION

The finite-element analysis and the response and damping calculation methods outlined in section 3 are first validated against experimental measurements (section 5.1). Thereafter, variation in damping with excitation amplitude, as well as parameters such as SMA wire area, wire length, wire angle relative to the beam, and tip mass are numerically examined. The pre-tension force in the SMA wires is selected to allow the wires to be strained inside the hysteresis loop, while ensuring that the beam does not buckle.

5.1. DESCRIPTION OF EXPERIMENT AND VALIDATION WITH TEST DATA

The experimental set-up used to validate the finite-element formulation is depicted schematically in Figure 7. The base of the set-up is a 1″ thick aluminum plate, fixed on a sturdy table. A net of holes is drilled on the surface of the plate to fix clamps and mountings. An additional plate is welded on the side to fix a shaker. As seen in the figure, two wire clamps, one beam clamp, and a system of pulleys are installed on the plate. The beam clamp holds an aluminum beam that has a mass attached at its end. The tip mass comprises steel slabs screwed on the beam. The SMA wires are clamped between the beam and the pieces of steel constituting the tip mass. The wires pass through the wire clamps installed on the base plate. These clamps can be tightened, holding the wires in place. After passing through the system of pulleys, the ends of the wires are attached to adjustable tip masses used to introduce pre-tension in the wires.

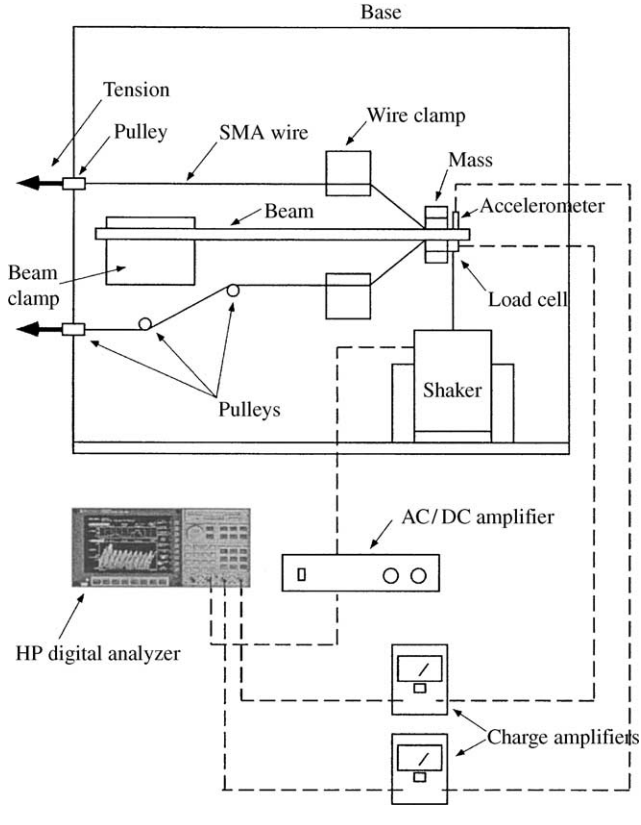

Figure 7. Schematic of experimental set-up.

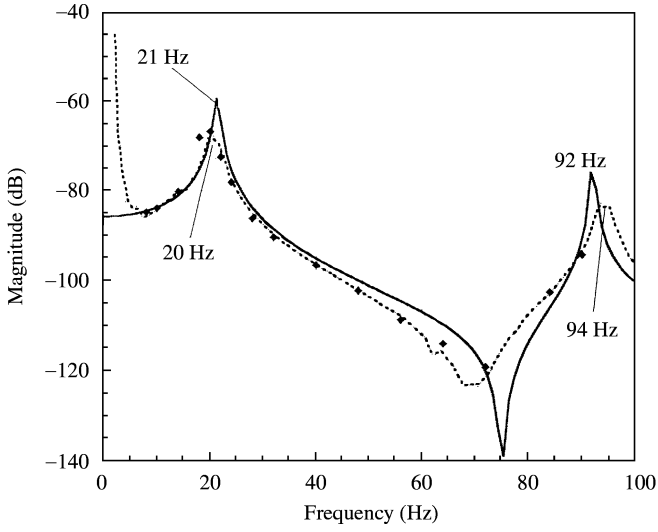

Figure 8. Frequency response function, validation of FEM simulation (——) with experimental data (– – –, random noise; ◆, sine dwell).

The shaker is connected to the beam tip by a "stinger" of low flexural stiffness and high axial compressive stiffness to decouple the structure from the rotary inertia of the shaker. A load cell is installed between the stinger and the structure to monitor the force input to the system. An accelerometer is placed on the other side of the beam, at the same axial location to monitor the acceleration near the tip of the beam in the transverse direction. The accelerometer and load cell signals are monitored using a digital signal analyzer and recorded for processing.

The system properties are given below: the aluminum beam has a length of 41 cm, a width of 48·4 mm, and a thickness of 5·05 mm. The SMA wires are 12·8 cm in length, 0·51 mm in diameter, are mounted at an angle of 19·1° relative to the beam, and have a pre-tension of 87 N. The tip mass is 1·22 kg and extends along the beam length from 35 to 38 cm. The shaker, load cell and accelerometer are connected 1 cm from the beam tip. The SMA wires were pre-cycled to approximately 400 stress/strain cycles (as suggested in reference [9]) at strain amplitudes corresponding to the maximum tip displacement available with the shaker, to stabilize the hysteresis behavior before collecting data.

Random noise tests as well as sine dwell tests were carried out. The amplitude of the compliance frequency response function is shown in Figure 8. The correlation between the finite-element predictions and experimental results is very good. Due to limitations of the shaker, large excitation input could not be achieved so results in Figure 8 do not display non-linear behavior associated with the amplitude-dependent modulus of the SMA wires.

For the correlation results in Figure 8, the values of SMA storage and loss modulus used in the finite-element analysis were $G' = 4{\cdot}15 \times 10^6$ psi and $G'' = 0{\cdot}15 \times 10^6$ psi (instead of $G' = 3{\cdot}85 \times 10^6$ psi and $G'' = 0{\cdot}11 \times 10^6$ psi, as seen in Figure 6(a)). The higher value for G' was used because of the lower ambient temperature during the beam vibration test (reference [9] suggests that G' at 70F is higher than that at 90F). The larger value of G'' used is meant to account for factors such as friction at the wire clamps, etc., in an approximate sense.

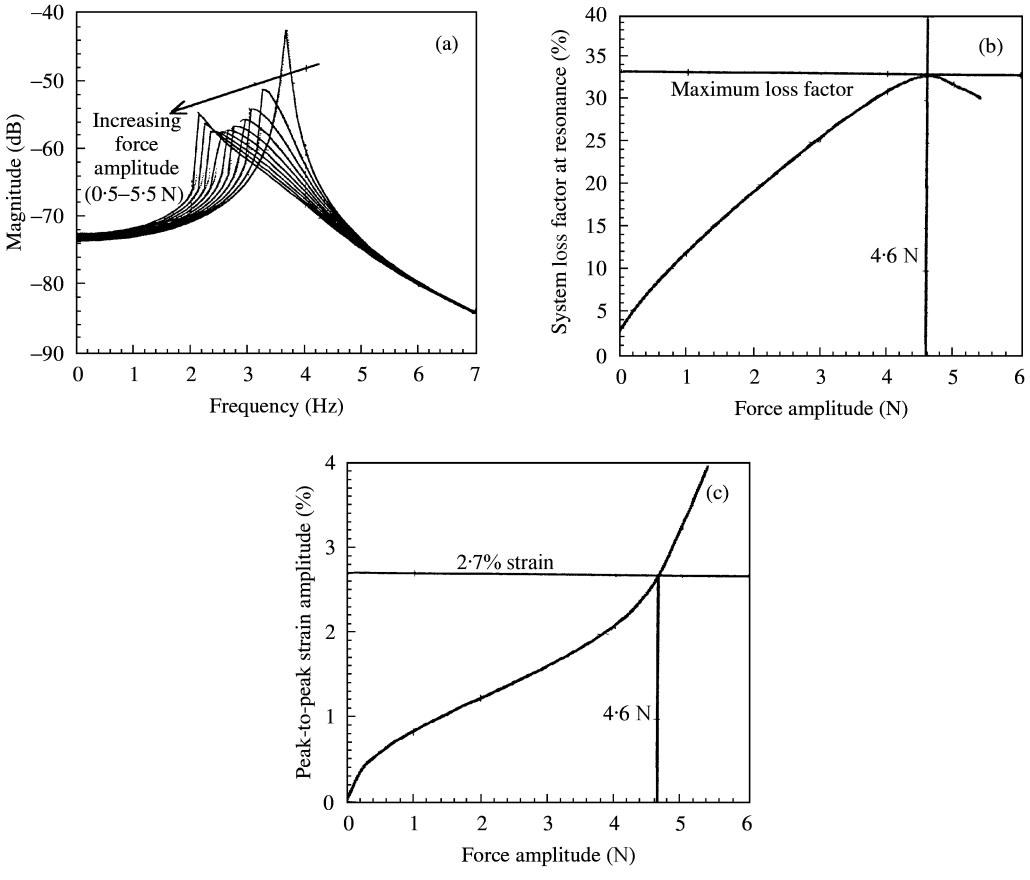

Figure 9. (a) Compliance response functions for increasing values of excitation amplitude, P_0; (*b*) *variation of modal damping versus excitation force amplitude*, P_0; (c) variation of SMA wire strain level at resonance versus excitation amplitude, P_0.

5.2. VARIATION IN EXCITATION-FORCE AMPLITUDE

Figure 9(a) shows compliance response functions corresponding to different excitation-force amplitudes. For the simulations in this section and in section 5.3, the following system properties are used: the beam length is 50 cm, width is 80 mm, and thickness is 3·5 mm. The SMA wires are 12·8 cm in length, have a cross-sectional area of 0·203 mm^2, are mounted at an angle of 20° relative to the beam, and have a pre-tension of 87 N. The tip mass is 14 kg and extends along the beam length from 40 to 47 cm. From Figure 9(a), it is seen that for larger excitation forces, the compliance response function clearly displays the characteristics of a non-linear softening system (since the SMA storage modulus decreases, Figure 6(a), implying that the wires "soften" at higher strain amplitudes), and the peak response is observed at lower frequencies. Figure 9(b) shows the variation in modal damping versus force amplitude. Damping is seen to increase upto a force amplitude of 4·6 N. Over this force amplitude range (0–4·6 N) the peak-to-peak strains in the SMA increase upto a level 2·7% (see Figure 9(c)). Recall from Figure 6(b) that the SMA wire loss factor increases significantly upto a peak-to-peak strain level of 2·7%, and decreases thereafter. Thus, when the force amplitude exceeds 4·6 N and peak-to-peak

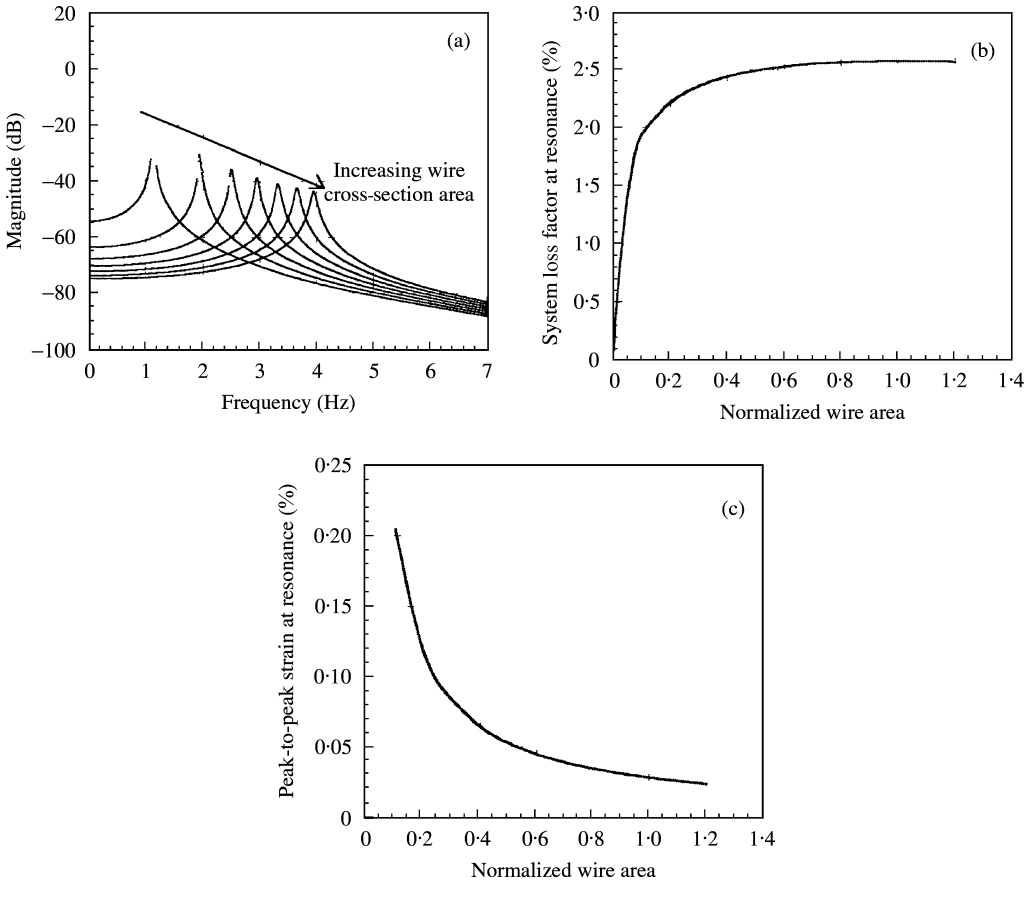

Figure 10. (a) Compliance response function for increasing SMA cross-section area; (b) variation of modal damping versus SMA wire cross-section area; (c) variation of SMA wire strain level versus SMA wire cross-section area; $P_0 = 0{\cdot}01$ N.

strains in the SMA wires exceed 2·7% the system damping reduces due to the decrease in the SMA wire loss factor. The increase in damping seen in Figure 9(b) (up to 4·6 N) causes reductions in the peaks of the compliance response function in Figure 9(a). The decrease in damping beyond 4·6 N causes the response peaks in Figure 9(a) to increase again.

5.3. INFLUENCE OF PARAMETER VARIATIONS ON MODAL DAMPING

5.3.1. *Influence of SMA wire cross-section area*

Figures 10(a) and 11(a) show compliance response functions, at low and high excitation-force amplitudes, respectively, for varying values of SMA wire cross-sectional area. In both figures, the system natural frequency is seen to increase as the wire area increases. This is reasonable as the system stiffness increases linearly as the wire area increases (see equation (16)).

Figure 10(b) shows the variation in modal damping versus SMA wire area (normalized by the baseline wire area) for low excitation-force amplitude, and Figure 10(c) shows

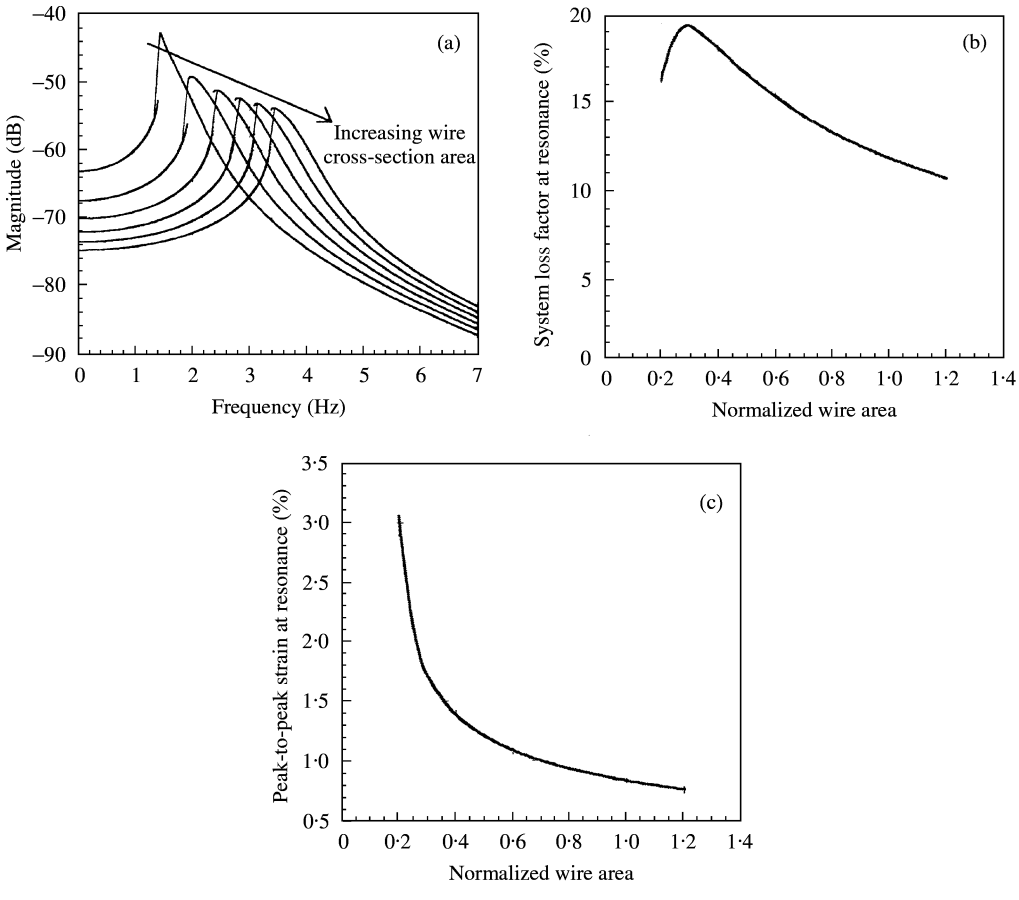

Figure 11. (a) Compliance response function for increasing SMA cross-section area; (b) variation of modal damping versus SMA wire cross-section area; (c) variation of SMA wire strain level versus SMA wire cross-section area; $P_0 = 1{\cdot}0$ N.

the corresponding variation in SMA peak-to-peak strain. Similar results for high excitation-force amplitude are shown in Figures 11(b) and 11(c). It should be recalled that the modal loss factor depends on the product of the SMA wire loss factor, η_{SMA}, and the strain energy ratio, U_{SMA}/U_{max} (equation (25)). At low force amplitudes, the SMA peak-to-peak strain shows little absolute variation with increasing wire area (Figure 10(c)). Thus, the SMA wire loss factor, η_{SMA}, is relatively unchanged, and it can be deduced that the increase in modal loss factor in Figure 10(b) is due to a corresponding increase in strain energy ratio. At a higher force amplitude, the SMA peak-to-peak strains sharply decrease between 3 and 0·75%, with increasing wire area (Figure 11(c)). A decrease in strain over this range corresponds to a sharp decrease in SMA wire loss factor, η_{SMA} (see Figure 6(b)). Then, the overall variation in modal damping seen with increasing wire area (Figure 11(b)) is a combination of an increase due to increasing strain energy fraction and a decrease due to a reduction in SMA wire loss factor.

5.3.2. *Influence of SMA wire length*

Figures 12(a) and 13(a) show compliance response functions, at low and high excitation-force amplitudes, respectively, for varying values of SMA wire length. In both figures, the system

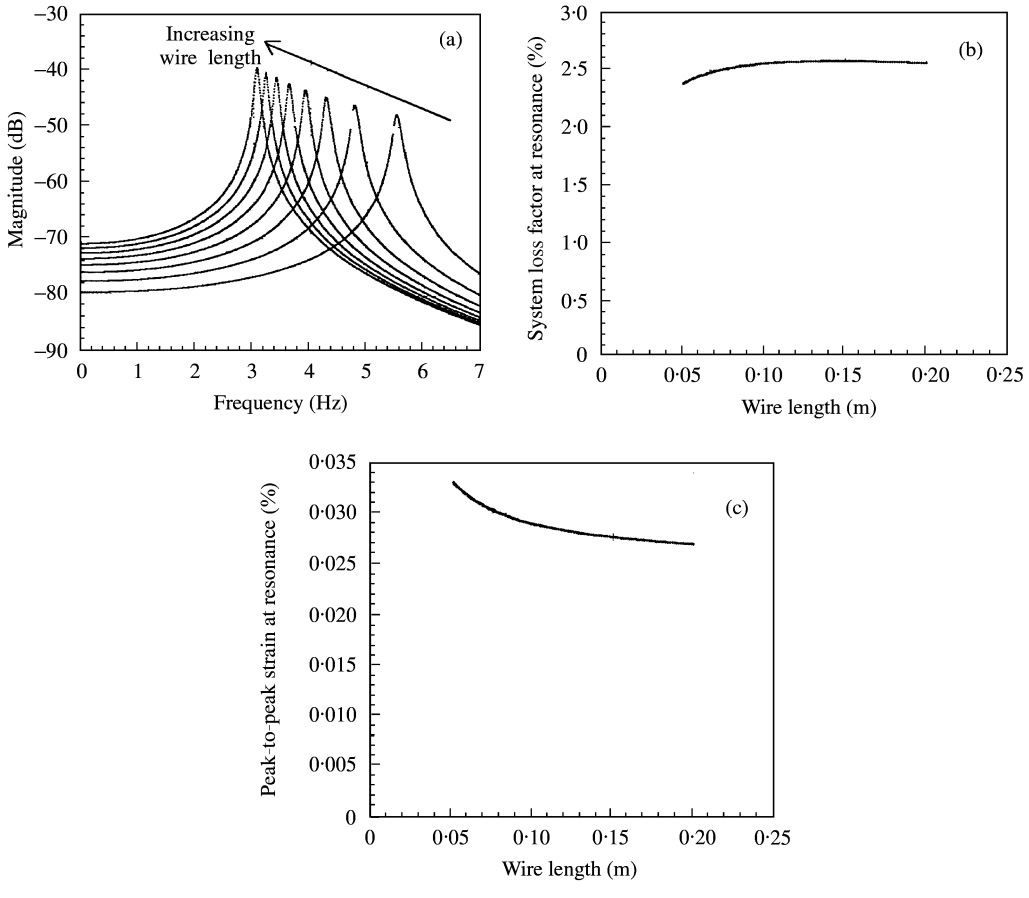

Figure 12. (a) Compliance response function for increasing SMA wire length; (b) variation of modal damping versus SMA wire length; (c) variation of SMA wire strain level versus SMA wire length; $P_0 = 0{\cdot}01$ N.

natural frequency is seen to decrease as the wire length increases. This is consistent with equation (16), which indicates that the influence of SMA wires on system stiffness is inversely proportional to the wire length.

Figures 12(b) and 13(b) show that for both low as well as high excitation-force amplitudes, the system damping has relatively low sensitivity to SMA wire length. The peak-to-peak strains in the SMA wire (Figures 12(c) and 13(c)) do not show much sensitivity to wire length either. Consequently, the SMA wire loss factor, η_{SMA} (which depends on the wire strain), does not vary significantly with wire length. Since the strain energy ratio, U_{SMA}/U_{max}, also has low sensitivity to wire length, it can be deduced from equation (25) that the overall system damping would not be highly sensitive to the SMA wire length.

5.3.3. *Influence of angle, θ, between SMA wires and beam*

Figures 14(a) and 15(a) show compliance response functions, at low and high excitation-force amplitudes, respectively, for varying values of the angle, θ, between the beam and the wires. From equation (16) it is seen that the influence of the wires on the system stiffness is dominated by the $\sin^2\theta$ term (the other terms are smaller since the beam is slender). Thus, as

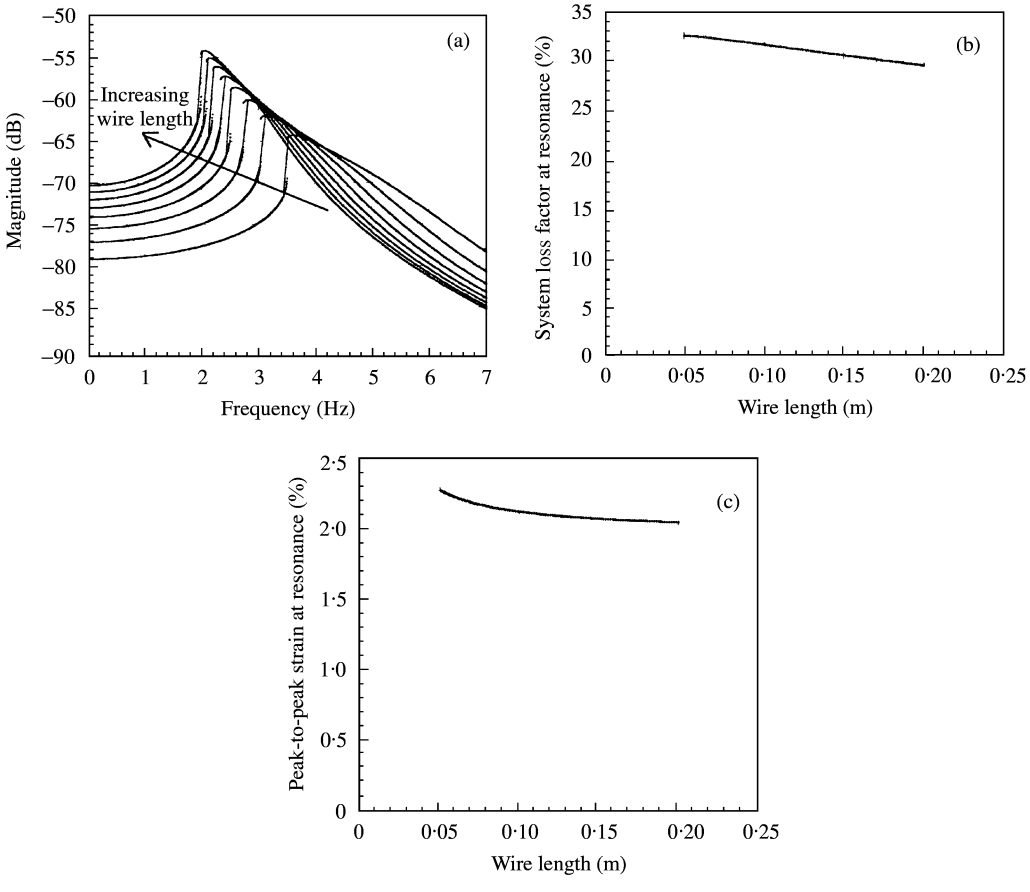

Figure 13. (a) Compliance response function for increasing SMA wire length; (b) variation of modal damping versus SMA wire length; (c) variation of SMA wire strain level versus SMA wire length; $P_0 = 4{\cdot}0$ N.

θ increases, the system stiffness increases, resulting in the increase in natural frequency seen in Figures 14(a) and 15(a).

Figures 14(b) and 15(b) show the variation in system damping versus θ, for low and high excitation-force amplitudes respectively. The corresponding peak-to-peak strain amplitudes in the SMA wire are shown in Figures 14(c) and 15(c). The strain levels in the wire are seen to decrease asymptotically with increasing θ, and show little change for values of $\theta > 30$ or 40°. Thus, the wire loss factor, η_{SMA}, is unchanged over this range, and it can be deduced that the decrease in system damping seen in Figures 14(b) and 15(b) must be associated with a reduction in the strain energy ratio, U_{SMA}/U_{max} (equation (25)). Figure 16 shows the mode shapes of the beam for wire angles of 15, 30 and 90° respectively. Clearly, as θ increases in the range of 30°–90°, the significant change in the mode shape (more curvature along the beam length for the same displacement at the point of attachment of the SMA wire) would result in a larger fraction of the strain energy being stored in the beam, and a smaller fraction in the SMA wires. At very low values of θ, the system damping could again decrease because the strain in the SMA wires *per unit tip displacement of the beam* is small (equation (9)). This is clearly seen at low force amplitudes (Figure 14(b)). At higher force amplitudes (Figure 15(b)), however, this effect appears to be compensated by the

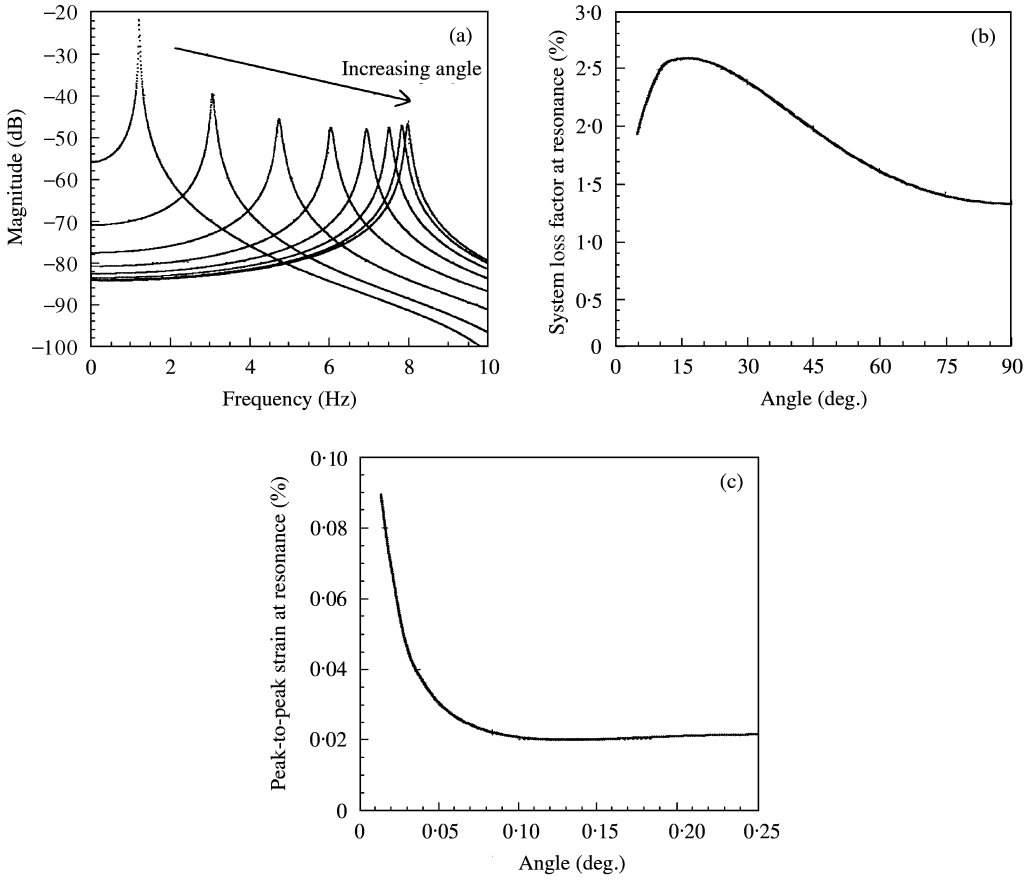

Figure 14. (a) Compliance response function for increasing angle, θ; (b) variation of modal damping versus angle, θ, between wire and beam; (c) variation of SMA wire strain level versus angle θ; $P_0 = 0{\cdot}01$ N.

increase in SMA wire loss factor, η_{SMA}, due to increased strain amplitude levels. An angle of around $\theta = 15^\circ$ between the wire and the beam appears to be optimal.

5.3.4. *Influence of tip mass*

Figures 17 and 18 show compliance response functions, at low and high excitation-force amplitudes, respectively, for increasing values of tip mass. In each of these figures, the system natural frequency is seen to decrease as the tip mass increases but the peak (resonant) response amplitude is independent of the tip mass. Thus, the tip mass has no influence on the operating peak-to-peak strain levels in the SMA wires or the operating wire loss factor, η_{SMA} (for a given force-excitation amplitude). Consequently, the system damping is also independent of the tip mass. For the two force-excitation amplitudes considered, the resonant peak-to-peak strains in the SMA wire are 0·026 and 2·15%, respectively, and the corresponding system loss factor values were 2·6 and 31·5%, respectively, *irrespective of the tip mass.*

6. SUMMARY AND CONCLUDING REMARKS

A finite-element analysis is developed of a clamped–free vibrating beam with a tip mass, and symmetrically mounted pseudoelastic SMA wires to introduce passive damping. The

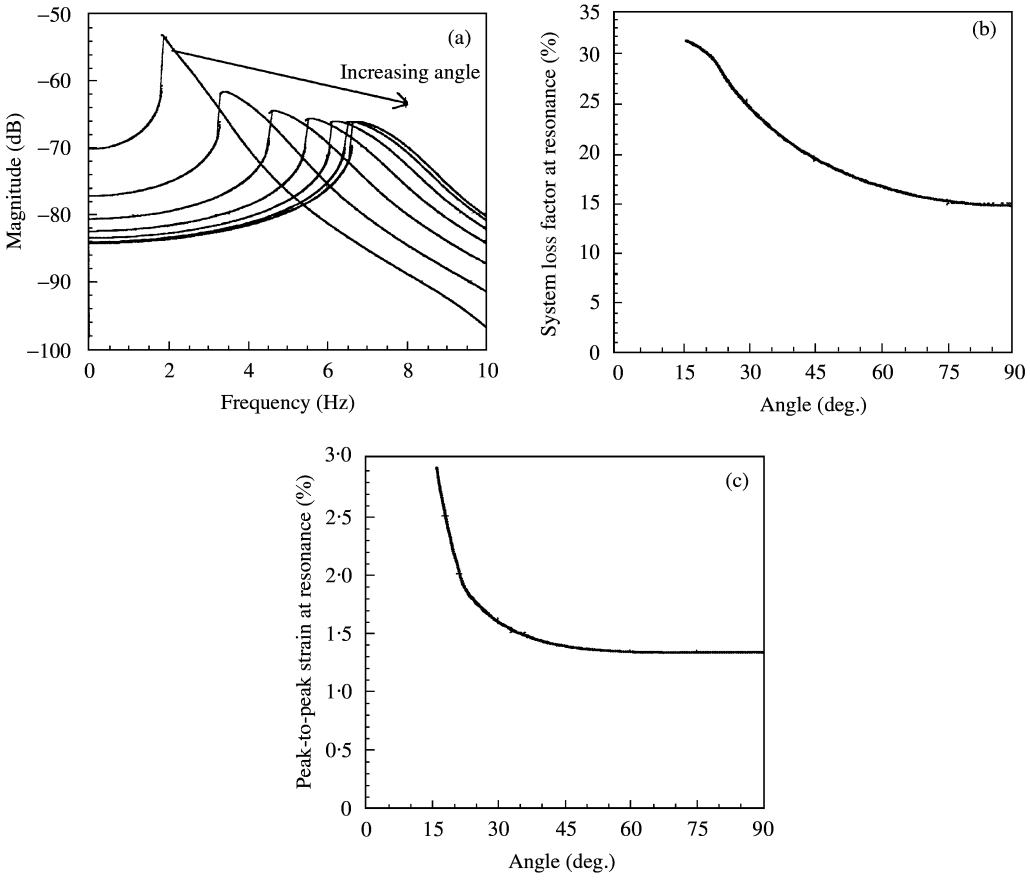

Figure 15. (a) Compliance response function for increasing angle, θ; (b) variation of modal damping versus angle, θ, between wire and beam; (c) variation of SMA wire strain level versus angle θ; $P_0 = 4{\cdot}0$ N.

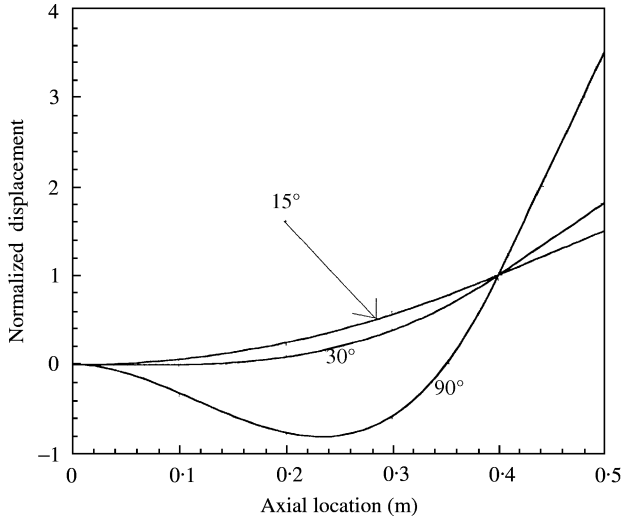

Figure 16. Mode shapes of the beam for different values of the angle, θ, between beam and wire.

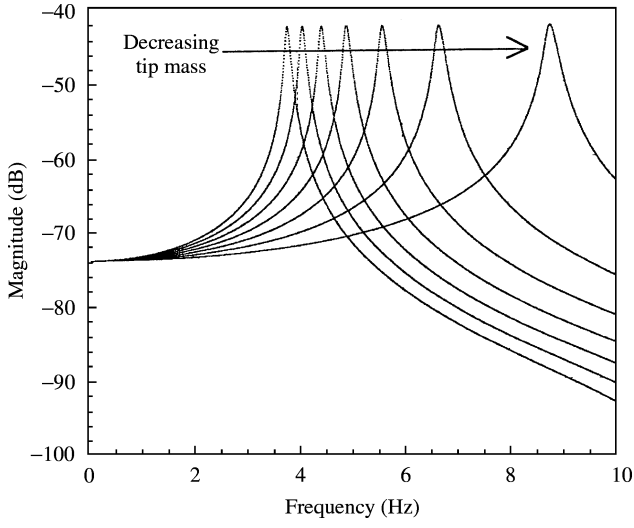

Figure 17. Compliance response function for increasing values of tip mass, $P_0 = 0{\cdot}01$ N.

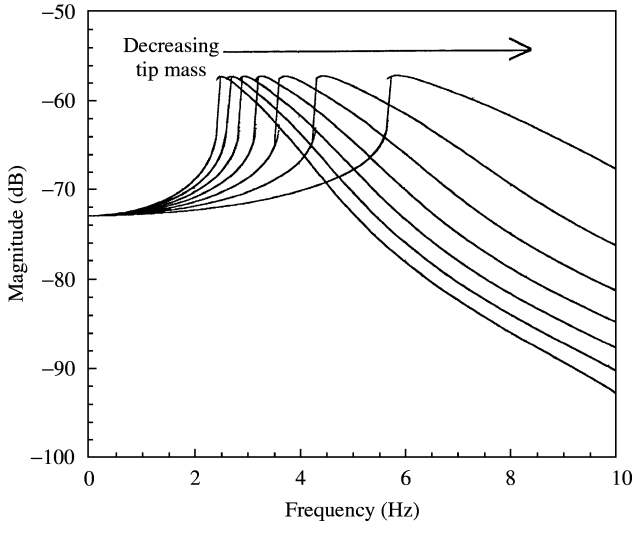

Figure 18. Compliance response function for increasing values of tip mass, $P_0 = 4{\cdot}0$ N.

finite-element results showed excellent correlation with experimental results. The SMA behavior is represented using an amplitude-dependent complex modulus (based on previously reported experimental data). The beam is subjected to a harmonic excitation force near the tip, and its bending response is calculated using the harmonic balance method. The response calculation is iterative on account of the non-linear behavior of the SMA wires. Damping in the fundamental mode of vibration is examined by considering the system loss factor at resonance. The effects of excitation-force amplitude, SMA wire cross-section area, wire length, the angle between the SMA wire and the beam, and the tip mass, on available damping, were examined in detail. The following observation were made:

(1) The *SMA wire loss factor* increases with strain amplitude up to about 2·7% peak-to-peak strain. Thus, in general, larger amount of damping is available at higher excitation–force amplitudes that produce operational strain amplitudes in the SMA wire around this range. In the present study, it was seen that modal loss factors varied from around 2·5% at low excitation-force amplitudes, to over 30% for high excitation levels.

(2) In addition to the operational SMA wire loss factor (which depends on the strain amplitude in the wire), system damping depends on the fraction of the strain energy in the SMA wire (relative to the total strain energy in the system). Higher values of this *strain energy ratio* result in better damping performance.

(3) *Dependence on SMA wire cross-section area*: at low excitation levels, more damping is available for larger wire cross-section area. However, at higher excitation levels, the damping may decrease with increasing cross-section area. This is because even though the strain energy ratio increases, there is a significant reduction in the SMA wire loss factor at the lower strain amplitudes obtained in the thicker (stiffer) wires.

(4) *Dependence on SMA wire length*: the damping level is only mildly sensitive to this parameter.

(5) *Dependence on the angle between the SMA wire and the beam*: the available damping is strongly dependent on this parameter, with the optimal value being in the range of 15–20°. For larger angles, the strain energy ratio reduces due to a significant change in the mode shape of the beam.

(6) The damping introduced in the system by the SMA wires is *independent of the tip mass.*

REFERENCES

1. D. E. Hodgson 1988 *Using Shape Memory Alloys*. Sunnyvale, CA: Shape Memory Applications, Inc.
2. D. Wolons, F. Gandhi and B. Malovrh 1998 *Journal of Intelligent Material Systems and Structures* **9**, 116–126. Experimental investigation of the pseudoelastic hysteresis damping characteristics of shape memory alloy wires.
3. J. A. Inaudi, J. M. Kelly, W. Taniwangsa and R. C. Krumme 1993 *Proceedings of Damping* '93, *San Francisco*, HAA-1–HAA-20. Analytical and experimental study of a mass damper using shape memory alloys.
4. P. R. Witting and F. A. Cozzarelli 1993 *Proceedings of Damping* '93, *San Francisco*, ECC-1–ECC-19. Design and seismic testing of shape memory structural dampers.
5. E. Rivin and L. Xu 1994 *Proceedings of the ASME, Materials for Noise & Vibration Control*, NCA-Vol. 18/DE-Vol. 80, 35–41. Damping of NiTi shape memory alloys and its application for cutting tools.
6. P. Thompson, G. I. Balas and P. H. Leo 1995 *Smart Materials and Structures* **4**, 36–41. The use of shape memory alloys for passive structural damping.
7. Y. C. Yiu and M. E. Regelbrugge 1995 *Proceedings of the 36th AIAA/ASME/ASCE/AHS/ASC Structures Structural Dynamics and Materials Conference*, 3390–3398. Shape memory alloy isolators for vibration suppression in space applications.
8. P. W. Clark, I. D. Aiken, J. M. Kelly, M. Higashino and R. C. Krumme 1995 *Proceedings of SPIE on Smart Structures and Materials* **2445**, 241–251. Experimental and analytical studies of shape memory alloy dampers for structural control.
9. D. Wolons 1997 *M.S. Thesis in Aerospace Engineering, The Pennsylvania State University*. An experimental investigation of the pseudoelastic damping characteristics of NiTi shape memory alloy wires.
10. K. Tanaka 1990 *Journal Pressure Vessel Technology* **112**, 158–163. A phenomenological description on thermomechanical behavior of shape memory alloys.
11. C. Liang and C. Rogers 1990 *Journal of Intelligent Material Systems and Structures* **1**, 207–234. One-dimensional thermomechanical constitutive relations for shape memory materials.

12. L. C. BRINSON 1993 *Journal of Intelligent Material Systems and Structures* **4**, 229–242. One-dimensional constitutive behavior of shape memory alloys: thermomechanical derivation with non-constant material functions and redefined martensite internal variable.
13. J. G. BOYD and D. C. LAGOUDAS 1994 *Proceedings of the ASME, Mechanics of Phase Transformations and Shape Memory Alloys*, AMD-Vol. 189/PVP-Vol. 292, 159–177. A constitutive model for simultaneous transformation and reorientation in shape memory materials.
14. B. J. LAZAN 1969 *Damping of Materials and Members in Structural Mechanics* Oxford: Pergamon Press; first edition.
15. A. D. NASHIF, D. I. G. JONES and J. P. HENDERSON 1985 *Vibration Damping* New York: John Wiley & Sons.
16. W. FLUGGE 1967 *Viscoelasticity*. New York: Blaisdell.
17. F. GANDHI and I. CHOPRA 1994 *Journal of the American Helicopter Society* **39**, 59–69. An analytical model for a nonlinear elastomeric lag damper and its effect on aeromechanical stability in hover.
18. F. GANDHI and I. CHOPRA 1996 *Journal of the American Helicopter Society* **41**, 267–277. Analysis of bearingless main rotor aeroelasticity using an improved time-domain nonlinear elastomeric damper model.
19. F. GANDHI and I. CHOPRA 1996 *Smart Materials and Structures* **5**, 517–528. A time-domain non-linear viscoelastic damper model.
20. F. GANDHI and D. WOLONS 1999 *Smart Materials and Structures* **8**, 49–56. Characterization of the pseudoelastic damping behavior of shape memory alloy wires using complex modulus.
21. G. CHAPUIS 1999 *M.S. Thesis in Aerospace Engineering, The Pennsylvania State University*. Use of pseudoelastic shape memory alloy wires for passive damping augmentation of a vibrating beam.